2020 IEEE International Conference on Robotics and Automation (ICRA)
31 May - 31 August, 2020. Paris, France

Mechanics for Tendon Actuated Multisection Continuum Arms

Phanideep S. Gonthina, Michael B. Wooten, Isuru S. Godage, and Ian D. Walker

***Abstract*—Tendon actuated multisection continuum arms have high potential for inspection applications in highly constrained spaces. They generate motion by axial and bending deformations. However, because of the high mechanical coupling between continuum sections, variable length-based kinematic models produce poor results. A new mechanics model for tendon actuated multisection continuum arms is proposed in this paper. The model combines the continuum arm curve parameter kinematics and concentric tube kinematics to correctly account for the large axial and bending deformations observed in the robot. Also, the model is computationally efficient and utilizes tendon tensions as the joint space variables thus eliminating the actuator length related problems such as slack and backlash. A recursive generalization of the model is also presented. Despite the high coupling between continuum sections, numerical results show that the model can be used for generating correct forward and inverse kinematic results. The model is then tested on a thin and long multisection continuum arm. The results show that the model can be used to successfully model the deformation.**

I. Introduction

Continuum (continuous backbone) robots possess theoretically infinite DoF (Degrees of Freedom) with respect to their flexible and smooth bending capability which would require large number of DoF to approximate with discrete rigid-linked arms [1]. But continuum arms achieve bending only with a finite number of DoF. Therefore, along with their flexibility, active bending along the entire length of the arm, straightforward down-scalability, and availability of various actuation methods continuum arms appear particularly suitable for navigation in congested environments.

There have been many continuum arm prototypes proposed over the years [2], [3], [4], [5], [6] and they successfully proved their versatility in field applications including inspection tasks [7], [8], [9]. Continuum arm designs and various actuation principles have found their way into minimally invasive surgical applications [10], [11], [12], [13], [14].

One of the most prominent types of continuum robot features remotely actuated tendons [15], [16], [17]. A long thin example of the tendon-actuated type featured in this paper, intended for inspection tasks in outer-space applications, was designed and developed [18] and is shown in Fig. 1b.

In contrast to rigid robotic arms (i.e., no link deformation during motion), modeling continuum arms is challenging and there are two main approaches; lumped approximation, and

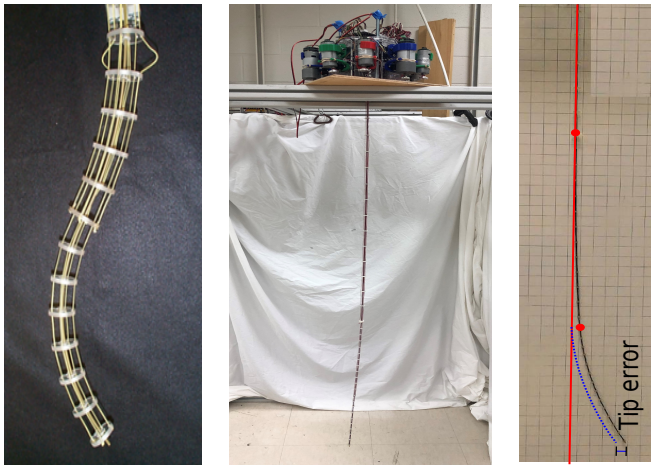

(a) (b) (c)

Figure 1: (a) Tendon-actuated continuum arm, (b) Long thin continuum robotic cable developed at Clemson University for inspection operations in highly constrained spaces, and (c) The coupling effect of tendon actuated continuum arms results in errors when modeled with length based models.

"true" continuum shape modeling [1]. Lumped approaches such as [5], [19] denote the natural transition from rigid-linked to continuum arm modeling but they require many virtual DoF to accurately represent continuum sections. Because of the redundancy, this poses computational problems particularly for inverse kinematics employing iterative methods. Chirikjian [20] and Mochiyama [21] pioneered the use of shape functions to parameterize spatial orientations of hyper-redundant robots. The curve parametric kinematic model in [22] formulates multisection continuum arm kinematics but does not account for the tendon length coupling. Tendon driven robot mechanics models in [3] considered both axial and bending deformations but the work was limited to planar, single continuum sections. Cosserat beam mechanics based models reported in [6], [23] also considered single continuum sections with no axial deformation. Further, applying length based models to robotic arms that exhibit significant passive axial deformations produces incorrect results because of the unaccounted backbone compression [18]. Additionally, due to force and kinematic coupling, i.e., when a distal section is actuated, the reaction forces in preceding sections affect the lengths and bending angles. This will not be reflected in length based models as shown in Fig. 1c[1] and cause tendon

P.S Gonthina, M.B Wooten, and I.D. Walker are with the Dept. of Electrical & Computer Engineering, Clemson University, Clemson, SC-29634-0915 ({pgonthi, mbwoote, iwalker}@clemson.edu)

I. S. Godage is with the School of Computing, DePaul University, Chicago, IL 60604 USA (e-mail: igodage@depaul.edu).

[1]Note that this error is resulting from a small bending angle. This error grows proportional to the bending angle.

slack, tangling, and introduce backlash [3], [24].

Webster and Jones presented a detailed review on the specifics of both multisection and concentric tube robots in [25]. Concentric tube continuum robots use translational and rotational DoF to cover their work-spaces. Also they have the advantage of being able to produce in small profiles especially to suit minimally invasive surgical requirements. Concentric tube robot translation is an active DoF and therefore offers limited to no axial compliance. In addition, the desired bending angle is achieved by matching the bending stiffnesses of adjacent pre-curved concentric tubes (by bending in different directions). Therefore, the model as is not directly applicable to continuum robots with active bending and passive axial compliance.

This paper proposes a new mechanics model for tendon driven multisection continuum arms. It combines the established, tendon length based, curve parametric formulation for continuum arms with the concentric tube mechanics models to derive an efficient, tendon force based, mechanics model. In order to realize this, the curve parameters are derived in tendon forces thus eliminating the length related issues. The model is then generalized and extended in recursive formulation. The numerical results show that the proposed model produces good results efficiently. Despite the high coupling observed in the manipulator, results also show that the model can be used successfully for robot shape control to achieve task-space operations. The experimental results conducted on a long and thin continuum arm show that the model can be used to successfully model the deformation.

II. Prototype Description

A. Design Objectives

The development of the proposed inspection robot in Fig. 1b was guided by the following set of design objectives. The robot was intended to help equipment inspection tasks in the international space station where the instrument cabinets are tightly arranged with depths exceeding 1 m with inter-cabinet spacing less than 0.02 m. Hence, high length/diameter ratio was required to reach farther within the constrained spaces with dimensional limits; diameter $\leq$0.015 m and length $\geq$1.2 m. The reliability and portability of the robot is another prime concern. Therefore mature electromechanical actuation was employed for the reasons of high weight to power ratio and compactness. To enhance reliability, the mechanical design needs to be simple. This criteria ensures the possible on-board repairs in an unlikely event of equipment failure.

B. Mechanical Design

The continuum robot design used herein has a tendon actuated, concentric tube backbone. The core of the backbone consists of three carbon fiber tubes the thinnest of which is in the tip section, and the thickest supports the base section. These placements allow for telescopic movement of the tip and middle sections relative to the base. On each section there are several 3D-printed spacers, which have at least 9 holes for the tendons and are spaced as evenly as possible.

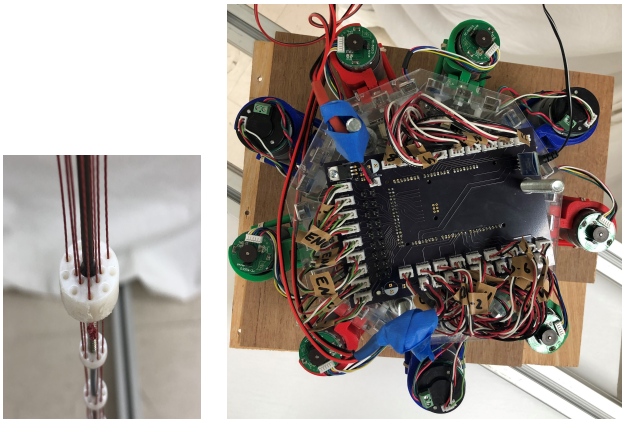

(a) (b)

Figure 2: (a) Spacer arrangement to guide the tendons to corresponding continuum sections, (b) Actuation package: Each tendon is operated by a high-torque servo motor.

Three tendons terminate at the tips of each section. This allows for two tendon-driven degrees-of-freedom per section, plus the telescopic degrees-of-freedom. The section lengths of the device shown are 0.219, 0.346, and 0.894 m for the tip, middle, and base sections respectively with a maximum spacer diameter of 0.016 m. The spacer and the tendon routing is shown in Fig. 2a.

C. Actuation Mechanism

The actuation package of the continuum arm is shown in Fig. 2b. It has nine DC motors controlled by a simple pd-controller based on encoder counts for those motors. They are connected to the microcontroller via motor driver and speed controlled using a PWM signal. Each motor rests on a load cell used to infer tension values in the tendons based on pressure on the load cell.

III. Methodology

In this section, the modeling challenges presented by the above design is first discussed through a single section model. The model is then generalized and extended to multisection continuum arms.

A. Mechanics of a Single Continuum Section

Continuum arm modeling via the curve parametric kinematics [22], [26] has the advantage over the lumped models because they use only the actual (local) DoF to model a continuum arm. This markedly improves the computational burden a lumped method has to encounter. A schematic of a single continuum section is shown in in Fig. 3a. Employing curve parametric kinematics it can be described by a varying curvature circular arc using following parameters; radius of curvature $\lambda \in (0, \infty)$, angle subtended by the bending arc $\phi \in [0, 2\pi_{max}]$, and angle of the bending plane with respect to the $+X$ axis, $\theta_i \in [-\pi, \pi]$. They are derived in variable length parameters as

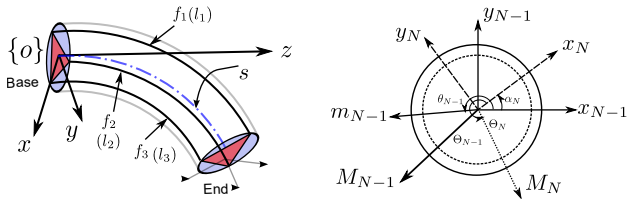

Figure 3: (a) Schematic of a single continuum section. Both tensile forces and length change variables are annotated for ease of reference, (b) Moment contribution from the N^{th} and $(N-1)^{th}$ continuum sections. N^{th} section effects are illustrated in dotted lines.

$$\lambda = \frac{(3L + l_1 + l_2 + l_3)\, r}{2\sqrt{l_1^2 + l_2^2 + l_3^2 - l_1 l_2 - l_1 l_3 - l_2 l_3}} \tag{1}$$

$$\phi = \frac{2\sqrt{l_1^2 + l_2^2 + l_3^2 - l_1 l_2 - l_1 l_3 - l_2 l_3}}{3r} \tag{2}$$

$$\theta = \arctan\left\{\sqrt{3}\,(l_3 - l_2)\,, l_2 + l_3 - 2l_1\right\} \tag{3}$$

where $L \in \mathbb{R}^+$ is the original length and $r \in \mathbb{R}^+$ is the radius of the continuum section. $l_j \in \mathbb{R}$ are the variable lengths of actuators and $j \in \{1, 2, 3\}$.

The length based model cannot be applied to the problem at hand because of the compression parameter missing among (1)-(3) [18]. To derive the compression, the tensile forces have to be measured. Therefore, it is justified to utilize the tendon tensile forces as the joint space for any tendon actuated continuum robot. Note that, it is straightforward to maintain the tendons in a desired tension (≥ 0) during operation employing simple force feedback mechanism [3].

Transforming the curve parameters from length variables to force variables is discussed in this section. Following reasonable assumptions are made without losing generality; (1) backbones follow circular arcs (verified in [3]), (2) linear elasticity in both axial and bending, (3) axial and bending strain are uniformly distributed across springs/backbone, (4) negligible friction between spacer discs and backbones, (5) and no gravity (the arm is intended to operate in outer-space). Note that, the last assumption also partially holds in terrestrial applications as the forces exerted in the lightweight arm are comparably smaller than the forces/moments applied by tendons to realize motion.

Let the corresponding force vector be $\boldsymbol{q} = [f_1,\, f_2,\, f_3] \in \mathbb{R}^3$. Without losing generality, we consider a tendril arm section that undergoes both linear and bending deformation. When tendons are actuated, let the length change and tension of any i^{th} tendon is related as

$$c\,(\boldsymbol{q}) + l_i\,(\boldsymbol{q}) = \alpha f_i \tag{4}$$

where c is the compression of the backbone, l is the length change, and α is some proportional coefficient. Note that, if the backbone length remain unchanged, $c\,(q) = 0$.

Substituting (4) into (3) yields

$$\theta\,(\boldsymbol{q}) = \arctan\left\{\sqrt{3}\,(f_3 - f_2)\,, f_2 + f_3 - 2f_1\right\} \tag{5}$$

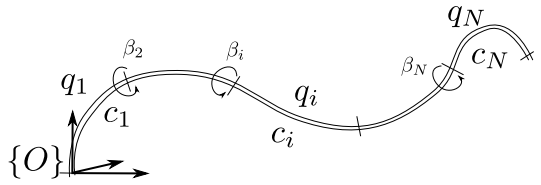

Figure 4: Arbitrarily long multisection continuum arm schematic.

Note that c and α get canceled indicating θ is independent from the compression.

Considering the cumulative tensile forces acting on the continuum section and curve parametric kinematics [26], the arc length, $s \in \mathbb{R}^+$, can be derived as

$$s\,(\boldsymbol{q}) = L + \tfrac{1}{3K}\,(f_1 + f_2 + f_3) \tag{6}$$

where $L \in \mathbb{R}^+$ is the original length of the section and $K \in \mathbb{R}^+$ is the linear stiffness coefficient. For fixed-length continuum arms, K will be very high.

The bending deformation is proportional to ϕ, s, and the bending stiffness coefficient, B. If the resultant torque acting on the arm tip is τ, then

$$\phi\,(\boldsymbol{q}) = \eta\frac{s\tau}{B} \tag{7}$$

where η is some proportional coefficient.

The resultant moment in θ direction can be related to individual tensile forces as

$$\frac{\tau}{r} = f_1 \cos(-\theta) + f_2 \cos\left(\tfrac{2\pi}{3} - \theta\right) + f_2 \cos\left(\tfrac{4\pi}{3} - \theta\right) \tag{8}$$

Deriving $\sin(\theta)$ and $\cos(\theta)$ from (5) and substituting in (8) results in $|\tau| = r\sqrt{f_1^2 + f_2^2 + f_3^2 - f_1 f_2 - f_1 f_3 - f_2 f_3}$. Applying τ in (7) gives

$$\phi\,(\boldsymbol{q}) = \eta\frac{rs}{B}\sqrt{f_1^2 + f_2^2 + f_3^2 - f_1 f_2 - f_1 f_3 - f_2 f_3} \tag{9}$$

Finally, from circular arc geometry, λ is computed as

$$\lambda\,(\boldsymbol{q}) = \frac{s\,(\boldsymbol{q})}{\phi\,(\boldsymbol{q})} \tag{10}$$

Now, the curve parameters derived herein in tensile forces (i.e $\boldsymbol{q}$) can be used to derive the homogeneous transformation matrix (HTM), $\mathbf{T} \in SE\,(3)$, of the continuum section as

$$\mathbf{T}\,(q) = \mathbf{R}_z\,(\theta)\,\mathbf{P}_x\,(\lambda)\,\mathbf{R}_y^T\,(-\phi)\,\mathbf{P}_x\,(-\lambda)\,\mathbf{R}_z^T\,(\theta) \tag{11}$$

where $\mathbf{R}_z \in SO\,(2)$, $\mathbf{R}_y \in SO\,(2)$ are rotational matrices about the Z and Y axes. $\mathbf{P}_x \in \mathbb{R}$ is the translation matrix along the +X axis [26].

B. Multisection Manipulator Model

As mentioned in Section I, the forces and moments of distal continuum sections affect the bending angles and compression in preceding sections. As a result, the single section curve parameters derived in Section III-A cannot be directly employed to model the curve parameters of proximal sections of a multisection continuum arm. Rather, the cumulative force and moments need to be considered in

the model to obtain the correct spatial orientations. In this section, a recursive formulation is proposed to compute the curve parameters for all the sections of an arbitrarily long general tendon operated continuum arm. Each section adopts the 3 DoF tendon mechanism to which the curve parameters were derived in Section III-A.

Figure 4 shows the schematic of an $N > 0$ section long continuum arm. The base section of the arm coincides with the task-space coordinate frame $\{O\}$. Any i^{th} continuum section is attached to the preceding $(i-1)^{th}$ section rigidly with a β_i angle offset to facilitate tendon routing without crowding. The corresponding force joint space vector is $q_i = [f_{i1},\, f_{i2},\, f_{i3}] \in \mathbb{R}^3$ and $q_i \leq 0$ to denote tensile forces being applied. The tendons are mechanically constrained to actuate at a distance r_i, parallel to the backbone (i.e., by using spacers). The actuator original length is L_{i0} and $f_{max} \leq f_{ij} \leq 0$; $j \in \{1, 2, 3\}$ is the actuator number. Note that $L_i > 0$ and $r_i > 0$ are constant design parameters. The linear and bending stiffness coefficients are respectively K_i and B_i. Let the curve parameters of each section without considering the coupling effects be λ_i, ϕ_i, and θ_i. The same with the coupling effects incorporated are Λ_i, Φ_i, Θ_i.

The distal most N^{th} section is only subjected to forces resulting from $\boldsymbol{q}_i$. Hence the curve parameters can be directly derived from the single section formulation given in section III-A. Continuum section $N-1$ is subjected to axial and bending deformation resulting from both $\boldsymbol{q}_i$ and $\boldsymbol{q}_{i-1}$. Taking $\boldsymbol{q}_i$ exerting on N^{th} section, the arc length of the $(N-1)^{th}$ section is given by

$$s_{N-1}\left(\boldsymbol{q}^N, \boldsymbol{q}_{N-1}\right) = L_{N-1} + \frac{F_N + \sum_{j=1}^{3} f_{(N-1)j}}{3K_{N-1}} \quad (12)$$

where $\boldsymbol{q}^i = [\boldsymbol{q}_i, \cdots, \boldsymbol{q}_N] \in \mathbb{R}^{3(N-i)}$ and $F_i = \sum_{k=i}^{N}\sum_{j=1}^{3} f_{kj}$. Note that $\boldsymbol{q}^i$ denotes the cumulative force variables from successive sections to the i^{th} section to account for the force and moment coupling.

Consider the schematic shown in Fig. 3b depicting the N^{th} and $(N-1)^{th}$ section moments. From (7) the moment $M_N = \Phi_N B_N$. The vector addition of moments gives the resultant torque, M_{N-1} and bending angle Θ_{N-1} as

$$B_{N-1}\Phi_{N-1}\cos\Theta_{N-1} = \eta_{N-1}s_{N-1}r_{N-1}G_{N-1}\cos\theta_{N-1} + B_N\Phi_N\cos\left(\Theta_N - \beta_N\right) \quad (13)$$

$$B_{N-1}\Phi_{N-1}\sin\Theta_{N-1} = \eta_{N-1}s_{N-1}r_{N-1}G_{N-1}\sin\theta_{N-1} + B_N\Phi_N\sin\left(\Theta_N - \beta_N\right) \quad (14)$$

where $G_i = \sqrt{f_{i1}^2 + f_{i2}^2 + f_{i3}^2 - f_{i1}f_{i2} - f_{i1}f_{i3} - f_{i2}f_{i3}}$.

The Φ_{N-1} is now computed from (13) and (14) by applying to the trigonometric identity $\cos^2\Theta_{N-1} + \sin^2\Theta_{N-1} \equiv 1$. By applying the resulting Φ_{N-1} into either (13) or (14), Θ_{N-1} can be derived. Utilizing Φ_{N-1}, s_{N-1} and the arc geometry, now Λ_{N-1} is computed as

$$\Lambda_{N-1}\left(\boldsymbol{q}^N, \boldsymbol{q}_{N-1}\right) = \frac{s_{N-1}\left(\boldsymbol{q}^N, \boldsymbol{q}_{N-1}\right)}{\Phi_{N-1}\left(\boldsymbol{q}^N, \boldsymbol{q}_{N-1}\right)} \quad (15)$$

Table I: Parameter values used in numerical computations

	L [cm]	r [mm]	K $\left[Nm^{-1}\right]$	B $\left[Nmrad^{-1}\right]$	β [rad]
Base	60	5	$1 \times 10^{6*}$	2.2	0
Mid	46	3	2×10^3	1.2	$\frac{2\pi}{9}$
End	34	2	6×10^2	0.12	$\frac{2\pi}{9}$

* The base section has no springs and therefore shows no axial deformation

These results can be generalized to implement a recursive scheme to compute the curve parameters of tendon actuated continuum arms with any number of sections. The computation is initiated at the N^{th} section with initial parameters $F_N = \sum_j^3 f_{Nj}$, $s_N = L_N + \frac{F_N}{K_N}$ from (6), $\Phi_N = \phi_N$ from (9), and $\Theta_N = \theta_N$ from (5).

C. Forward and Inverse Kinematics

Once the curve parameters in tensile force variables are derived for each section, they can be utilized to derive the HTM of the entire arm as

$${}_0^N\mathbf{T}\left(Q\right) = \prod_{i=1}^{N}\left(\mathbf{T}_i\mathbf{T}_{Ji}\right) = \begin{bmatrix} \mathbf{R} & \boldsymbol{p} \\ 0 & 1 \end{bmatrix} \quad (16)$$

where $Q = \left[\boldsymbol{q}_1,\, \boldsymbol{q}_2,\, \ldots,\, \boldsymbol{q}_{N-1}, \boldsymbol{q}_N\right] \in \mathbb{R}^{3N}$ is the composite joint space variable of the arm, $\mathbf{T}_{Ji} \in SE\left(3\right)$ are the HTM's of continuum section joint offsets, $\mathbf{R} \in SO\left(3\right)$ is the rotational matrix and $\boldsymbol{p} \in \mathbb{R}^3$ is position vector of the arm tip.

Because of the redundancy of general multisection continuum arms, inverse kinematics rely on iterative methods which are based on the manipulator Jacobian matrix, $\mathbf{J} \in \mathbb{R}^{3\times 3N}$ to relate task-space and joint space velocities [27]. The linear velocity along the neutral axis with reference to $\{O\}$, denoted by $\upsilon \in \mathbb{R}^3$, is given by

$$\upsilon\left(Q, \dot{Q}\right) = \mathbf{J}\left(Q\right)\dot{Q} \quad (17)$$

IV. Simulation Results

In this section, numerical results utilizing the proposed force based mechanics model are presented. Firstly, the results on how the new model successfully accounts for the coupling is demonstrated. Then inverse kinematic solutions are presented for two spatial trajectory tracking examples. These exhibit the proposed model's ability to generate versatile spatial operation even with highly coupled tendon actuated systems. The parameter values used in the simulations are listed in Table I with proportional scalars assumed unity for this work. Note that, when all actuation forces of any continuum section are equal, it results in a kinematic singularity, i.e., $\lambda \to \infty$. But in this model, this can be trivially avoided by applying a small force (i.e., 0.1N) to one of the joint space variable of the distal section. Because of the force coupling, this causes an insignificant bending in all preceding sections thus eliminating possible numerical problems.

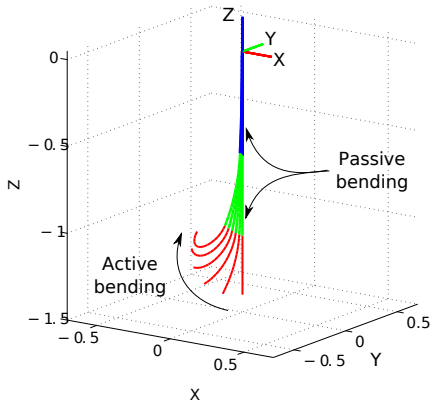

Figure 5: Illustration of the force and moment coupling. The distal section is intentionally bent via applying tension forces at the respective tendons. But the force transmitted to the preceding sections causes them to bend as well.

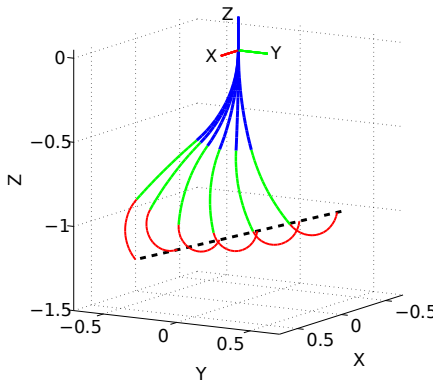

Figure 6: Linear spatial trajectory tracking example. Inverse mechanics solutions were solved utilizing the numerical approximations of the manipulator Jacobian.

A. Forward Kinematics

In this numerical result, to demonstrate the force and moment coupling effect of cable driven multisection continuum arms, an increasing tensile force is applied to f_{31} joint variable. In case of an uncoupled model, only the distal section would bend without affecting the preceding sections. The results obtained using the proposed model is shown in Fig. 5. It can be seen that the model correctly accounts for the transferred forces and moments to mid and base sections. Because of the substantial difference in bending and linear stiffness coefficients, the effects are limited. These results are carried out in the Matlab numerical environment.

B. Inverse Kinematics and Trajectory Tracking

The versatility of the proposed model for highly coupled, tendon actuated continuum-style inspection robots is demonstrated by following two spatial trajectory tracking examples. The spatial trajectories are computed via the inverse kinematics. Closed form inverse kinematic solutions for task-space position of multisection continuum arms are computationally infeasible. Therefore iterative procedures based on the multivariate Newton-Raphson approach are utilized to solve inverse kinematic problems [28]. The pseudo inverse of the Jacobian matrix, $\mathbf{J}^{\dagger} = \mathbf{J}^{T}\left(\mathbf{J}\mathbf{J}^{T}\right)^{-1}$, is implemented into the inverse kinematic algorithm due to its simplicity and efficiency. However, because of the high coupling between continuum sections, computing the end effector Jacobian is not trivial. Therefore, it is numerically approximated at the point of interest by using central differences formula with 10^{-3} step size and then the pseudo inverse is calculated.

In the first example, the arm tip follows a linear spatial trajectory starting at $[-.05, 0.4, -1]$ to $[0.5, -0.4, -1.2]$. The algorithm calculates 150 intermediate trajectory points, and the solutions for each point is found iteratively. The trajectory following is shown in Fig. 6. This gives a smooth joint-space solution as seen in the accompanying video. Since the proposed model benefits from the curve parametric implementation (in force-space), it is highly computationally efficient (produce results in 10s of milliseconds) in contrast to previous lumped models. For ease of comparison, the trajectory is drawn in a dotted line. The simulation result is also included in the accompanying video. For ease of comparison, the trajectory is drawn in dotted lines.

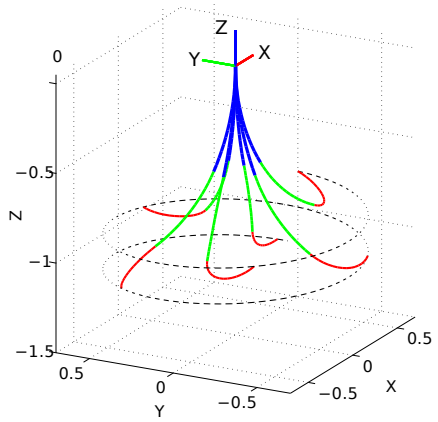

Figure 7: Spatial helical trajectory tracking.

The second example depicts the arm tip following a helical path given by the parametric equation $[0.7\cos(4\pi t), 0.7\sin(4\pi t), -1.2 + 0.4t]$ and $t \in [0, 1]$. Similar to the previous example, 150 equidistant points were generated between the starting and termination points to which the inverse kinematic solutions were computed utilizing MATLAB®'s "fmincon" constrained optimization routine.. The results are illustrated in Fig. 7. For ease of comparison, the trajectory is drawn in dotted lines. The full simulation is included in the supplementary video. The results show that the arm tip successfully tracks the given trajectory.

V. Experiment Results

In this section the model was utilized to perform a recursive scheme to compute the curve parameters of the thin long continuum robot with 3 sections detailed in Section II. A single Base section tendon was actuated with varying tension values. The position and tension values for three different configurations shown in Fig. 8 were recorded. The position data calculated by using 2 cameras on the X and Y axis

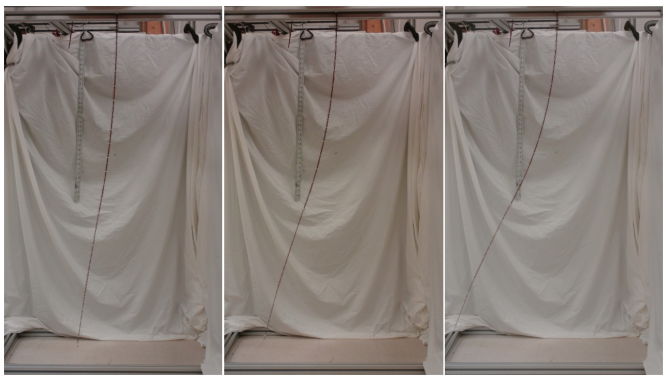

Figure 8: (a) Configuration-1 (b) Configuration-2 (c) Configuration-3

Table II: Results

	B1 $[Nmrad^{-1}]$	B2 $[Nmrad^{-1}]$	B3 $[Nmrad^{-1}]$	B4 $[Nmrad^{-1}]$	offset [rad]	RMS error $meters$
Congif 1	0.3433	0.4549	0.0782	0.7044	0.3883	0.0171
Config 2	0.3778	0.4158	0.0272	0.6643	0.2732	0.0125
Congif 3	0.3396	0.4421	0.0179	0.6482	0.247	0.0173

and 36 points were selected manually (one on each spacer in the image) and converted from pixel to meters using a pre-calculated conversion factor.

Known parameters such as the section radii, length, tension and position were substituted to define the static model in terms of bending stiffness and offset values. The offset value is the difference between the nominal angle and the actual bending plane angle calculated by the position data from the experiment. This offset was added to (5) to generate (18).

$$\theta\left(\boldsymbol{q}\right) = \tan^{-1}\left\{\sqrt{3}\left(f_3 - f_2\right), f_2 + f_3 - 2f_1\right\} + \text{offset} \quad (18)$$

An optimization routine using MATLAB®'s "`GlobalSearch`" and "`fmincon`" was then performed to find the stiffness and offset to give us the optimal agreement.

An initial cost function was calculated using three tip position values of each section. Torsion and non-constant curvature were observed and a 2-segment model for base section was implemented. A 3D polynomial curve of order 3 was fit to these four points using MATLAB®'s "`polyfit`" function and 25 points were generated. A cost function was thus implemented to calculate the RMS error of 15 points on the Base section, 6 on the Mid and 4 on the Tip section. The top and side view of the model fit for the three configurations in Fig. 8 are shown in Fig. 9, 10 and 11.

The numerical results for the three configurations are shown Table II. The bending stiffness values of the 4 segments are denoted by B1, B2, B3 and B4. B1 and B2 are for the first and second segments of the Base section, B3 for the Mid section and B4 for the Tip section. The bending stiffness and offset values are consistent for varying tension values.

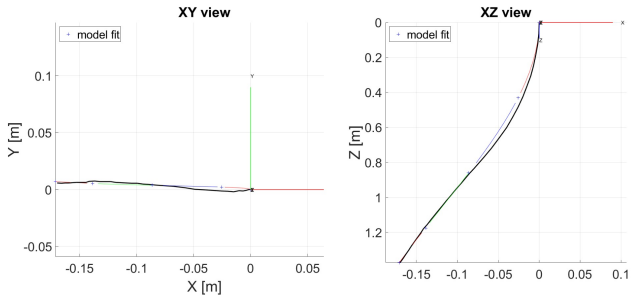

Figure 9: Top view (left) and Side view (right) of model fit for Configuration-1. Experiment data shown in black.

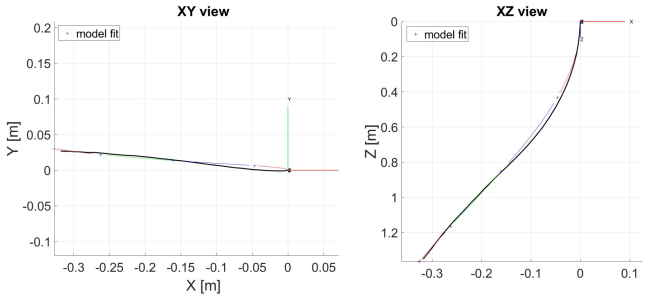

Figure 10: Top view (left) and Side view (right) of model fit for Configuration-2. Experiment data shown in black.

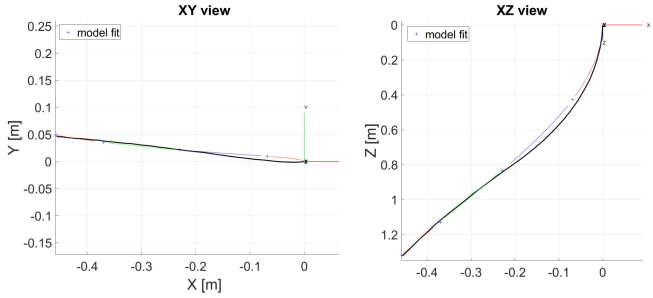

Figure 11: Top view (left) and Side view (right) of model fit for Configuration-3. Experiment data shown in black.

VI. Conclusions

Tendon length, force, and torque coupling in tendon-driven multisection continuum arms complicates the formulation of accurate mechanics models. Without accurate models, there can be slack cables and backlash. This can lead to tendon twisting, tangling and deviation from the intended shape. Motivated by these problems, this paper proposed a new general mechanics model for multisection continuum arms. The model was formulated recursively for easy extension to any continuum arm configuration. The model uses the actuation tensile forces as the joint space and marries length curve parametric and concentric arm models. The model was able to incorporate the coupled force and torque effects. Experiments were carried out to simulate the coupling effects in forward kinematics and trajectory following in inverse kinematics. Despite the high coupling, the model was able to produce results efficiently and to generate smooth trajectories.

Acknowledgments

This work was supported in part by U.S. National Science Foundation Grants IIS-1718075, IIS-1718755, IIS-1527165, and in part by NASA under contract NNX12AM01G.

REFERENCES

[1] G. Robinson and J. B. C. Davies, "Continuum robots-a state of the art," in *IEEE Int. Conf. on Robotics and Automation*, 1999, pp. 2849–2854.

[2] I. S. Godage, G. A. Medrano-Cerda, D. T. Branson, E. Guglielmino, and D. G. Caldwell, "Modal kinematics for multisection continuum arms," *Bioinspiration & Biomimetics*, vol. 10, no. 3, p. 035002, may 2015. [Online]. Available: https://doi.org/10.1088%2F1748-3190%2F10%2F3%2F035002

[3] D. Camarillo, C. Milne, C. Carlson, M. Zinn, and J. Salisbury, "Mechanics modeling of tendon-driven continuum manipulators," *IEEE Transactions on Robotics*, vol. 24, no. 6, pp. 1262–1273, 2008.

[4] M. A. Csencsits, "Operational strategies for continuum manipulators," Master's thesis, 2007.

[5] W. Rone and P. Ben-Tzvi, "Continuum robot dynamics utilizing the principle of virtual power," *IEEE Transactions on Robotics*, vol. 30, no. 1, pp. 275–287, Feb. 2014.

[6] D. C. Rucker and R. J. Webster, "Statics and dynamics of continuum robots with general tendon routing and external loading," *IEEE Transactions on Robotics*, vol. 27, no. 6, pp. 1033–1044, 2011.

[7] C. Li and C. D. Rahn, "Design of continuous backbone, cable-driven robots," *Journal of Mechanical Design*, vol. 124, no. 2, pp. 265–271, 2002.

[8] W. McMahan, V. Chitrakaran, M. A. Csencsits, D. M. Dawson, I. D. Walker, B. A. Jones, M. B. Pritts, D. Dienno, M. Grissom, and C. D. Rahn, "Field trials and testing of the octarm continuum manipulator," in *IEEE Int. Conf. on Robotics and Automation*, 2006, pp. 2336–2341.

[9] D. Palmer, S. Cobos-Guzman, and D. Axinte, "Real-time method for tip following navigation of continuum snake arm robots," *Robotics and Autonomous Systems*, vol. 62, pp. 1478–1485, 2014.

[10] J. Burgner-Kars, D. Rucker, and H. Choset, "Continuum robots for medical applications: A survey," *IEEE Transactions on Robotics*, vol. 31, pp. 1261–1280, 2015.

[11] N. Simaan, R. Taylor, and P. Flint, "A dexterous system for laryngeal surgery," in *IEEE Int. Conf. on Robotics and Automation*, 2004, pp. 351–357.

[12] R. J. Webster III, "Design and mechanics of continuum robots for surgery," Ph.D. dissertation, 2008.

[13] P. E. Dupont, J. Lock, B. Itkowitz, and E. Butler, "Design and control of concentric-tube robots," *IEEE Transactions on Robotics*, vol. 26, no. 2, pp. 209–225, 2010.

[14] R. S. Penning and M. R. Zinn, "A combined modal-joint space control approach for continuum manipulators," *Advanced Robotics*, vol. 28, no. 16, pp. 1091–1108, 2014.

[15] S. K. M.T. Chikhaoui, S. Lilge and J. Burgner-Kahrs, "Comparison of modeling approaches for a tendon actuated continuum robot with three extensible segments," *IEEE Robotics and Automation Letters*, vol. 4, no. 2, pp. 989–996, 2019.

[16] M. M. Dalvand, S. Nahavandi, and R. D. Howe, "An analytical loading model for$n$-tendon continuum robots," *IEEE Transactions on Robotics*, vol. 34, no. 5, pp. 1215–1225, Oct 2018.

[17] K. Oliver-Butler, J. Till, and C. Rucker, "Continuum robot stiffness under external loads and prescribed tendon displacements," *IEEE Transactions on Robotics*, vol. 35, no. 2, pp. 403–419, April 2019.

[18] M. M. Tonapi, I. S. Godage, and I. D. Walker, "Design, modeling and performance evaluation of a long and slim continuum robotic cable," in *IEEE/RSJ Int. Conf. on Intelligent Robots and Systems*, 2014, pp. 2852–2859.

[19] N. Giri and I. D. Walker, "Three module lumped element model of a continuum arm section," in *IEEE/RSJ Int. Conf. on Intelligent Robots and Systems*, 2011, pp. 4060–4065.

[20] G. S. Chirikjian and J. W. Burdick, "Kinematics of hyper-redundant manipulators," in *Proc. 2nd Int. Workshop on Advances in Robot Kinematics, Linz*, 1990, pp. 392–399.

[21] H. Mochiyama, E. Shimemura, and H. Kobayashi, "Shape control of manipulators with hyper degrees of freedom," *The International Journal of Robotics Research*, vol. 18, no. 6, pp. 584–600, 1999.

[22] B. A. Jones and I. D. Walker, "Kinematics for multisection continuum robots," *IEEE Transactions on Robotics*, vol. 22, no. 1, pp. 43–55, 2006.

[23] F. Renda, M. Giorelli, M. Calisti, M. Cianchetti, and C. Laschi, "Dynamic model of a multibending soft robot arm driven by cables," *IEEE Transactions on Robotics*, vol. 30, no. 5, pp. 1109–1122, 2014.

[24] W. McMahan, B. A. Jones, and I. D. Walker, "Design and implementation of a multi-section continuum robot: Air-octor," in *IEEE/RSJ Int. Conf. on Intelligent Robots and Systems*, 2005, pp. 2578–2585.

[25] R. Webster and B. Jones, "Design and kinematic modeling of constant curvature continuum robots: A review," *The International Journal of Robotics Research*, vol. 29, no. 13, pp. 1661–1683, 2010.

[26] I. S. Godage, E. Guglielmino, D. T. Branson, G. A. Medrano-Cerda, and D. G. Caldwell, "Novel modal approach for kinematics of multisection continuum arms," in *IEEE/RSJ Int. Conf. on Intelligent Robots and Systems*, 2011, pp. 1093–1098.

[27] J. M. Selig, *Introductory robotics*, 1st ed. Prentice Hall, 1992, vol. 5.

[28] S. R. Buss, "Introduction to inverse kinematics with jacobian transpose, pseudoinverse and damped least squares methods," Oct. 2004. [Online]. Available: http://math.ucsd.edu/~sbuss/ResearchWeb/ikmethods/iksurvey.pdf